Ultramicroscopy 32 (1990) 69–79
North-Holland

QUANTITATIVE ENERGY-FILTERED IMAGE ANALYSIS IN CYTOCHEMISTRY
II. Morphometric analysis of element-distribution images

C.W.J. SORBER

AEM Unit, Clinical Pathological Institute I, Erasmus University Rotterdam, P.O. Box 1738, 3000 DR Rotterdam, The Netherlands

J.B. VAN DORT

Hogeschool West-Brabant, Sector Laboratorium Onderwijs, Etten-Leur, The Netherlands

P.C. RINGELING, M.I. CLETON-SOETEMAN

Chemical Pathological Laboratory, Erasmus University Rotterdam, P.O. Box 1738, 3000 DR Rotterdam, The Netherlands

and

W.C. DE BRUIJN *

AEM Unit, Clinical Pathological Institute I, Erasmus University Rotterdam, P.O. Box 1738, 3000 DR Rotterdam, The Netherlands

Received at Editorial Office 18 September 1989; presented at Workshop June 1989

A combination of energy-filtered electron microscopy (EFEM) and an image-analysis system (IBAS/2000) is used for a morphometric analysis of chemical reaction products in cells. Electron energy-loss spectroscopic element-distribution images are acquired from cytochemical reaction products in a variety of cellular objects: (1) colloidal thorium particles in extra-cellular coat material, (2) iron-containing ferritin particles in liver parenchymal cells, (3) barium-containing reaction products in endoplasmic reticulum stacks, (4) elements present in lysosomal cerium- and barium-containing precipitates connected with acid phosphatase (AcPase) or aryl sulphatase (AS) enzyme activity. Areas or area fractions are determined from such element-distribution images by application of an objective image segmentation method. By superposition of two or more element-distribution images, mutual element relations are qualitatively established in lysosomal cerium- and barium-containing precipitates connected with acid phosphatase (AcPase) or aryl sulphatase (AS) enzyme activity. By comparing electron spectroscopic images (ESI) with element-distribution images, the mutual contrast per element relations are quantitatively investigated. The obtained gain in resolution in such electron energy-loss spectroscopic element-distribution images will be explained and discussed.

1. Introduction

To monitor, for integrated cytochemical and morphometric image analysis, changes in cytochemical product volume, attention has to be paid to the morphometric determination of area or area fractions in element-distribution images. In addition to the qualitative information about mutual element relations, the relation of the area(s) occupied by the element(s) to the total area of the item of interest (IoI) has to be established.

The recently introduced energy-filtered electron microscopy (EFEM) [1–8] potentially allows morphometric analysis of element-distribution images and image integration of element-distribution images to those defined by contrast (ESI).

* To whom correspondence should be addressed.

In this paper net-intensity element-distribution images will be morphometrically analyzed with the use of an image analyzer (IBAS 2000, Zeiss-Kontron), in a type of post-acquisition digitization. Element net-intensity image acquisition has been used before in TEM [1–5,7,8] and STEM [6,11–14]. Quantification of such images is considered to be rather complicated, because spectrum deconvolution is still a subject of investigation [9–10].

We use in our work a two-window method proposed before [2,15], which leads to semi-net-intensity element-distribution images, until programs are installed in our computer for multi-window subtraction procedures. Morphometric analysis of such semi-net-intensity element-distribution images will be performed by an objective segmentation method similar to that proposed for the ESI images [11].

Colocalization of elements introduced by multiple cytochemical reactions will be investigated by superposition of semi-net-intensity images [3,12].

Finally, the area of a lysosome acquired by contrast ($\Delta E = 250$ eV) will be determined and, by combining ESI images with element-distribution images, the sum-area of all elements enclosed will be compared with the area acquired by contrast.

The anticipated gain in chemical spatial resolution of EFEM over electron probe microanalysis (EPMA) [13] will be demonstrated and the improvement of the morphometric accuracy obtained by EFEM (as compared to EPMA) will be discussed.

2. Materials and methods

The instrument used for this investigation is a Zeiss EM 902 transmission microscope with an integrated electron energy filter according to Castaing–Henry–Ottensmeyer. Images are transferred to an image analyzer (IBAS 2000 Zeiss-Kontron, Oberkochen, FRG) by a TV camera for further analysis, processing or storage by normal routine (IBAS-Kontron) software. TEM images are directly recorded on film (Kodak SO163, The Hague, NL).

To collect chemical information, electron energy-loss spectra from small specimen areas are acquired by a photomultiplier (PMT). Spectra are visualized directly on a plotter or are fed into a personal computer (Olivetti M 280).

The spectra are beam intensity records versus energy loss (ΔE) from 0 to 2000 eV. While recording the spectrum, the narrow energy-selecting slit is projected on the PMT entrance diaphragm. A pre-chosen energy band (e.g. 100–200 eV wide) is seemingly moved over the energy-selecting slit, actually by changing the high tension (e.g. from 80 750 to 80 950 eV) over a constant (but adjustable) time interval. Only elements present in the irradiated area with energy losses within that band appear, generally with an intensity edge on a steadily decreasing continuum of inelastically scattered electrons.

Spectra have a twofold use: (a) for elemental identification in the irradiated IoI and (b) for image formation in the following way. Structure-sensitive ESI images are acquired at an energy loss $\Delta E = 250$ eV with an energy width of 20 eV. Similarly, two ESI images are formed around the ionization edge of the element of interest, one below the edge called the PIE (pre-ionization edge) image and one beyond the ionization edge called the IE (ionization edge) image. All images are transferred to the IBAS 2000 by a TV camera. A PIE image is subtracted, pixel by pixel, from the IE image to obtain a (semi-)net-intensity element-distribution image.

In some cases, images are shifted to compensate for some specimen drift between acquisition of the two images. The formation of zero-loss images has been described earlier [11].

Materials are derived from:
(a) human vaginal epithelial cells reacted with colloidal thorium to visualize acid mucopolysaccharide negatively charged ligands [16–18],
(b) rat iron-loaded liver parenchymal cells [19],
(c) aldehyde-fixed mouse peritoneal resident macrophages (MPrM) [20,21].

Integrated morphometric, multi-element analyses are performed with MPrM cell populations, treated with three simultaneously performed cytochemical reactions to detect different enzyme activities within one cell. Enzyme-related precipi-

tates expected to be detected, differentiated and measured are:
(a) barium and sulphur from aryl sulphatase (AS) activity in rough endoplasmic reticulum (RER) stacks and lysosomes,
(b) cerium and phosphate from acid phosphatase (AcPase) activity in lysosomal precipitates,
(c) platinum di-amino-benzidine (DAB) complexes from endogenous peroxidase (PO) activity in erythrocytes, endoplasmic reticulum and nuclear envelopes, lysosomes and eosinophil granules (see for cytochemical procedures refs. [20–23]).

All microscopic and section conditions are as described in the preceding paper [11].

Averaged (100 ×), shading-corrected, element-related PIE and IE images are acquired from the various ionization edges of the elements involved (Th, Fe, Ba, Ce, P, S). The PIE and IE grey-value intensities of the surroundings of the cells are matched visually by the use of a look-up table (in which case grey values are transformed to colors). Subsequently, image segmentation is performed, by a method similar to that described for ESI images at $\Delta E = 250$ eV [11]. This method is based upon the use of a frequency histogram of the semi-net-intensity image for objective segmentation between the area occupied by the element and its surroundings. This procedure leads to a true binary image. By comparing the number of pixels present inside binary IoI's with the total number in a cell or frame, the relative area can be obtained. Images of a grating replica acquired under the same conditions are used to convert relative to real areas or real lengths. To eliminate unwanted (noise) remnants in the picture, the IBAS function SCRAP is used.

Binary element-related images are given pseudo colors for better presentation or, for example, to emphasize colocalization visually. The resultant images are recorded from the screen on color film (Ektachrome).

Colocalization, defined by a simultaneous occurrence of pixels at the same place in two images, is established by superposition of an ESI and an element-distribution image, or alternatively, of two or more element-distribution images, by the Boolean operator (X)OR and adapting the pseudo colors accordingly.

3. Results

Morphometric analysis is divided in two main parts: single net-intensity element-distribution images and multiple net-intensity element-distribution images.

For morphometric analysis of single element-distribution images, three examples will be described. The particle area (diameters) will be measured in binary images from (a) monomorphic colloidal-thorium particles in a cell coat at the cell surface; whereas the area fractions will be determined for two different situations: (b) for monomorphic particles present in cells in a tissue, (c) for heteromorphic particles present in single cells.

3.1. Monomorphic particles at a cell surface

In fig. 1, the reaction of the acid mucopolysaccharide ligands in the cell coat with positively charged colloidal thorium particles is shown. The PIE image (fig. 1a) shows the visual absence of colloidal particles. In the IE image (fig. 1b) the presence of the colloidal particles is evident. In the inset of fig. 1a, a thorium spectrum is shown from the extra-cellular colloidal thorium particles. The absence of sulphur is indicated; the presence of carbon is shown. In fig. 1b, the area in which the particles are measured at higher magnification is framed. The mean particle diameter measured from the binary net-intensity thorium images was 2.44 ± 0.33 nm ($n = 65$). The mean minimum particle diameter was 1.60 nm. The shape factor was 0.65, and the morphometric accuracy 25 pixels/particle.

3.2. Monomorphic particles in cells in a tissue

In fig. 2, ferritin particles present in rat liver parenchymal cells are shown. Fig. 2a shows the acquired net-intensity iron-distribution image of the lysosomal and cytoplasmic area. Fig. 2b shows part of a spectrum, between 680 and 740 eV, from the iron-containing lysosome. The circle indicating the irradiated lysosomal area is to scale. The 20 eV wide energy bands used for the PIE and IE images are indicated. Fig. 2c shows the zero-loss image

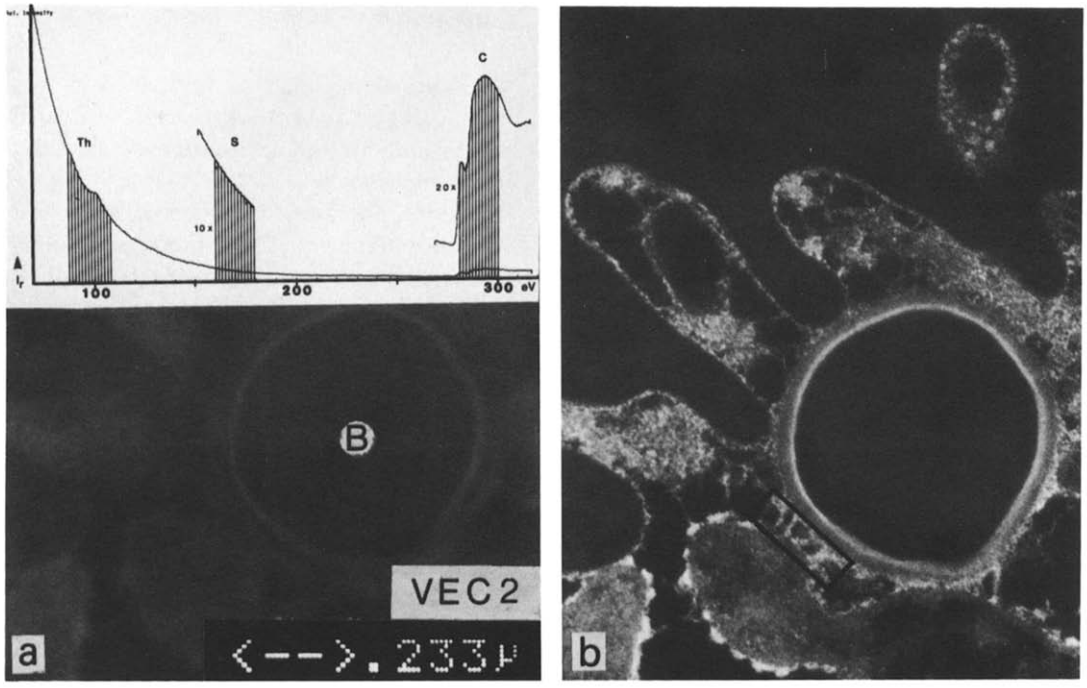

Fig. 1. Colloidal thorium particles reacted with acid mucopolysaccharides in the cell coat from human vaginal epithelial cells (VEC). (a) Pre-ionization edge image (PIE); B indicates a bacterium present in that habitat. (b) Ionization edge image (IE) at $\Delta E = 88$ eV. In the inset in (a) a spectrum of the colloidal thorium product is shown plus the width of the thorium window. In (b) the area is indicated in which the diameter of the colloidal thorium particles is measured at high magnification. Bar indicates 230 nm.

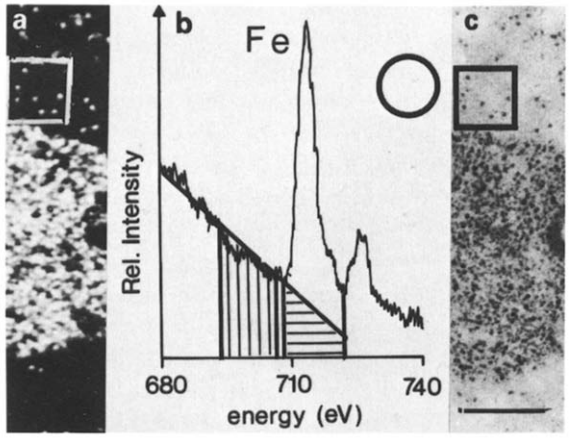

Fig. 2. Cytoplasmic and lysosomal ferritin particles in a rat liver parenchymal cell. (a) Iron net-intensity image. (b) Spectrum of a lysosomal ferritin containing area. The PIE (|||) and IE (≡) windows are indicated. The circle represents the analyzed area to scale. (c) Zero-loss image. The square areas in (a) and (c) indicate identical cytoplasmic ferritin iron cores. Bar indicates 270 nm.

from the same site. In the square areas in figs. 2a and 2c, single iron cores are marked. To determine the area fraction of ferritin particles in iron-loaded rat liver parenchymal cytoplasm, iron net-intensity images are acquired from randomly chosen cytoplasmic areas at constant magnification. In that case the frame area is the reference area. Cytoplasmic ferritin particles are initially assumed to be sufficiently separated to be measured individually. We used the first derivative of the grey-value frequency histogram for objective segmentation as described before [11]. In the cytoplasmic areas the total area of the ferritin iron-core particles is measured. As the total area of the frame is known, the ferritin iron-core area fraction can be determined (2.758×10^{-3}).

In addition, the number of iron-core particles per cytoplasmic area is determined with the IBAS program COUNT. The mean ferritin iron-core particle area is subsequently established by divid-

ing the total particle area by the number of particles. Assuming the cytoplasmic iron cores to be spherical, the averaged mean core diameter is calculated from 19 (0.54 μm^2) cytoplasmic fields, leading to a mean value for ferritin iron cores of 5.93 ± 0.46 nm (morphometric accuracy = 54 pixels/Fe core, shape factor = 0.8139, $n = 2400$ particles).

3.3. *Irregularly shaped particles*

Barium precipitates in intracellular rough endoplasmic reticulum stacks are measured in a similar

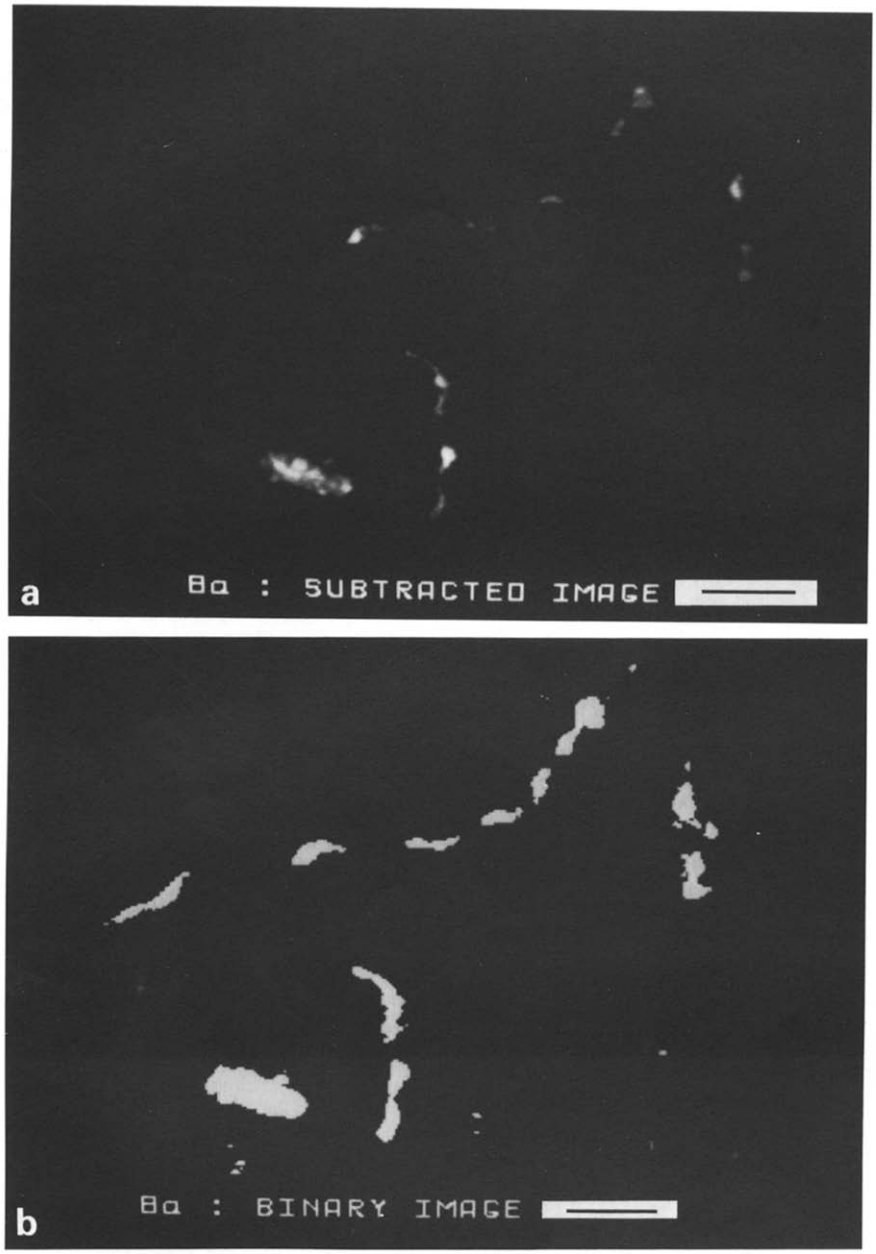

Fig. 3. Barium precipitates in the endoplasmic reticulum stacks in MPrM cells. (a) Barium net-intensity image, (b) binary image after objective segmentation. Bar indicates 150 nm.

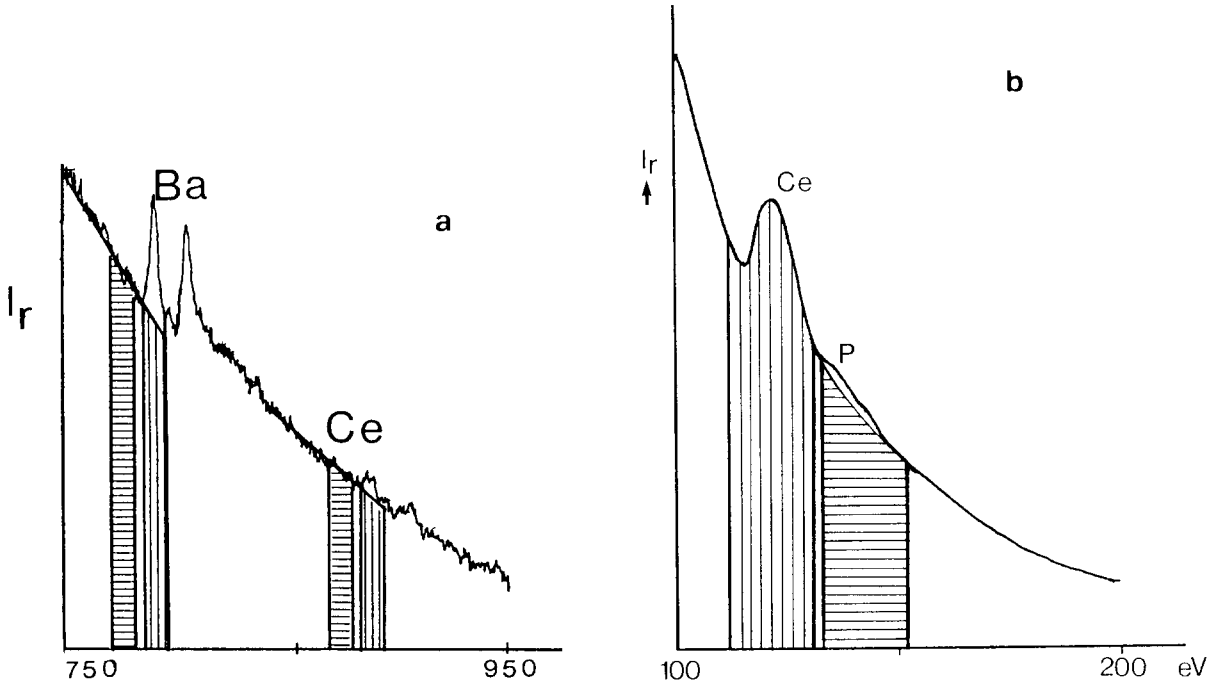

Fig. 4. Spectra from a multiple element-containing lysosomal precipitate. In (a) the presence of barium and cerium are indicated and the PIE (≡) and IE (|||) windows. In (b) the phosphorus edges are shown plus the cerium $N_{4,5}$ edges and the phosphorus PIE (|||) and IE (≡) windows.

way as described for ferritin iron cores. The net-intensity barium image is shown in fig. 3a. The net-intensity barium image is segmented and the binary image is shown in fig. 3b. In the binary image the total barium-containing area is determined. Then the total area cross section of the cell is determined (see color plate in the preceding paper [11], fig. 8a), and the area fraction of this precipitate is calculated (1.5×10^{-3}).

The morphometric analysis of multiple element semi-net-intensity images is shown in figs. 4 and 5.

In fig. 4a, part of a spectrum ($\Delta E = 750$–950 eV) is shown from a lysosomal area (232 nm^2) containing barium and cerium. Very much smaller edges have been obtained from phosphorus between $\Delta E = 100$ eV and 200 eV (fig. 4b), whereas a sulphur edge failed to show up clearly. In figs. 5a–5h, a lysosomal AS-derived barium sulphate precipitate is used to demonstrate that when in a spectrum a clear ionization edge is present, (IE) – (PIE) subtraction procedures result in a bright image (figs. 5d, 5f and 5h) comparable to the ESI image at $\Delta E = 250$ eV (fig. 5b). When in the spectrum an edge is absent (e.g. the sulphur peak at $\Delta E = 164.8$ eV) the resultant image after a similar subtraction operation (figs. 5c, 5e and 5g)

Fig. 5. Multiple images from the same MPrM-cell lysosome in which it will be shown that subtraction of the PIE image (d) from the IE image (f) results in a bright image (barium net-intensity image (h)) which in intensity is comparable with the $\Delta E = 250$ eV ESI image (b), provided clear edges are present in the spectrum (see fig. 4a). When in the spectrum edges are absent, like for sulphur (fig. 4b), IE – PIE subtraction (e) – (c) gives a resultant image with black "holes", which is comparable with the zero-loss image (a). The bar given in (b) indicates 550 nm and pertains to all figures. (c) PIE image of sulphur $\Delta E = 144$ eV + 20 eV. (d) PIE image of barium $\Delta E = 761$ eV + 20 eV. (e) IE image of sulphur $\Delta E = 184$ eV + 20 eV. (f) IE image of barium $\Delta E = 801$ eV + 20 eV. (g) Difference image (IE – PIE) of sulphur showing the absence of any semi net-intensity sulphur as black holes. (h) Difference image (IE – PIE) of barium showing the presence of semi net-intensity of barium as white particles. In (c)–(f) the ionization edges (IE and PIE) are incorrectly abbreviated as absorption edges (AE and PAE).

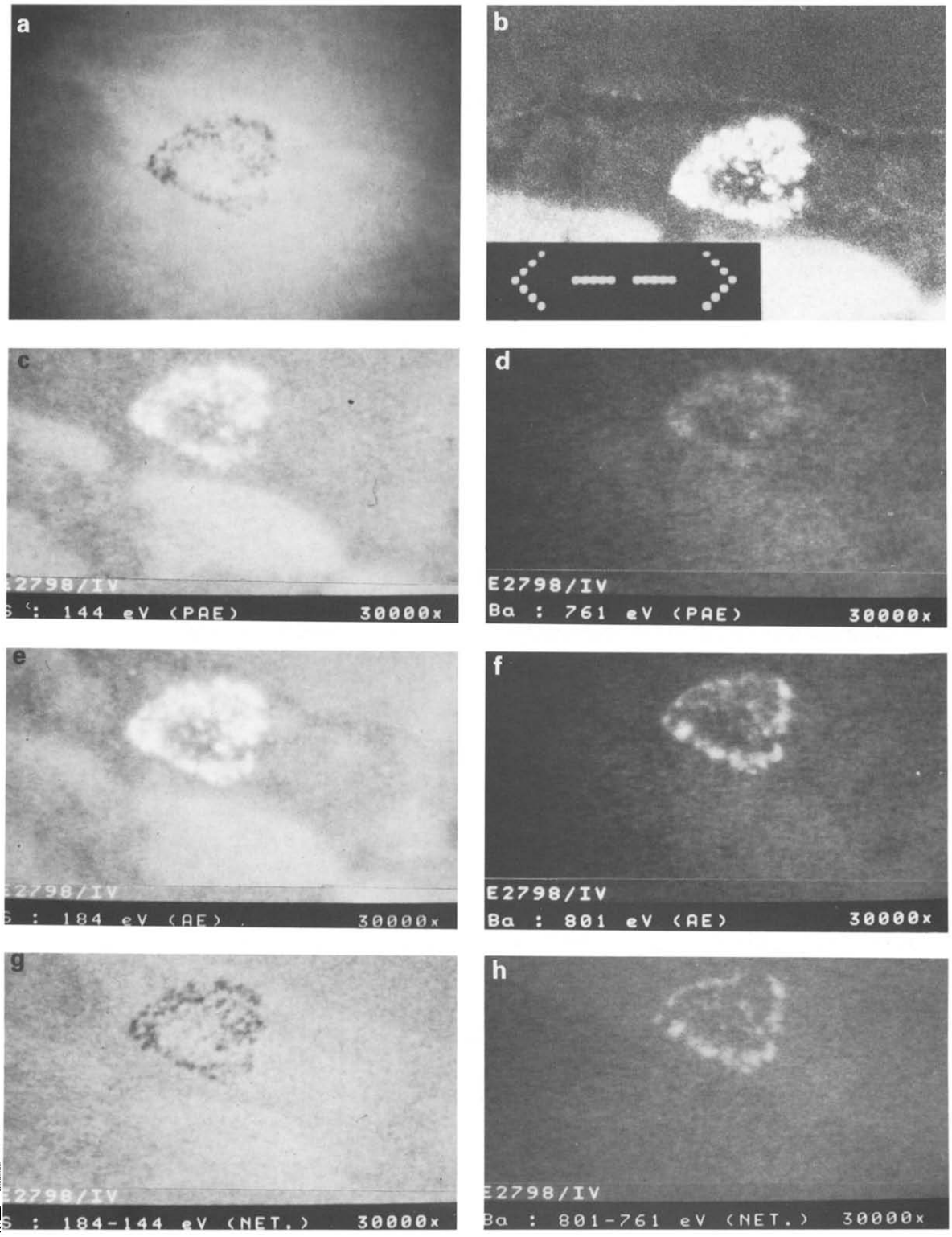
a
b
c
2798/IV
144 eV (PAE) 30000x
d
E2798/IV
Ba : 761 eV (PAE) 30000x
e
2798/IV
184 eV (AE) 30000x
f
E2798/IV
Ba : 801 eV (AE) 30000x
g
2798/IV
184-144 eV (NET.) 30000x
h
E2798/IV
Ba : 801-761 eV (NET.) 30000x

shows black holes, comparable to the particles in the zero-loss image (fig. 5a).

Spectral information (fig. 4a) indicated already the co-occurrence of AcPase-related cerium phosphate and AS-related barium in the analyzed lysosomal area. From all three elements involved (barium, cerium and phosphorus) element-distribution images are acquired as described above.

From each element-distribution image, binary images are obtained by frequency histogram-based segmentation. These images are collected in the color plate in ref. [11]: figs. 8c–8h, page 64. In figs. 8c, 8e and 8g, binary distribution images are shown from the individual elements in pseudo colors.

To demonstrate the presence or absence of colocalization, we used superposition of two images and new bright pseudo colors (white, yellow) were attached to the pixels the two element images had in common (figs. 8d, 8f and 8h of ref. [11]). In this particular case, cerium and phosphorus were expected to be found in register, whereas barium (and sulphur) preferably should be located at a different place. In figs. 8c and 8e, cerium and phosphorus are depicted separately. In fig. 8d, these images are combined visualizing both elements coincided. In fig. 8g, the presence of barium is shown. In fig. 8f, cerium and barium images are superimposed showing the virtual lack of coincidence by the absence of the yellow color. In fig. 8h, cerium, phosphorus and barium are superimposed to show some additional (undesired) coincidence between barium and phosphorus.

Morphometric analysis also results in area fractions from these irregularly shaped lysosomal element-containing particles (see figs. 8a and 8b of ref. [11]).

By converting relative area into real area, two particle areas are obtained from the same lysosome. ESI-image segmentation (fig. 5b) results in an area of 23480 nm^2. The area occupied by summation of all element binary images (fig. 8h of ref. [11]) is 23020 nm^2, lacking 360 nm^2 ($= \pm 1.5\%$). As an element-distribution image of the peroxidase-related platinum-containing poly-DAB reaction product is not acquired, theoretically the missing area could be occupied by this reaction product.

4. Discussion

In the previous paper [11], the influence of the image mode used, the integration frequency and the aperture (5, 10 and 20 mrad) are investigated with regard to their effects upon contrast. Two morphometric parameters related to contrast (area and perimeter) are determined from ESI images. Element-distribution images are generally acquired with a 90 μm objective diaphragm (20 mrad).

A two-population Gaussian distribution is obtained in the frequency histogram of element-distribution images which similarly can be used for an objective segmentation procedure. Limitations encountered with our segmentation procedure based upon contrast, described before for ESI images, are not different from the ones encountered for element-distribution images.

Recently Trebbia [24] indicated that the degree of confidence to be achieved about the IoI's absence or presence in final images can be defined by the signal-to-noise ratio (SNR) (see also Egerton [10]). He warned not to easily accept the presence of elements at sites where they are expected. Trebbia considers the two-window acquisition procedure for net-intensity element-related images followed in this paper inappropriate. However, when edges are high (as in cytochemical precipitates) and the IE window in the energy spectrum is at a large distance from the origin (Fe = 708 eV, Ba = 781 eV, Ce = 883 eV) subtraction of the PIE image from the IE image may be acceptable. We realize that this aspect is more complicated and needs further investigation, hence we call our resultant images "semi-net-intensity images", to indicate our awareness of the restriction. Correct procedures for quantification of EEL spectra have been outlined [9,10,25]. However, until our computer is able to calculate the true continuum under the element-related edge in the IE window, we have to use the method demonstrated.

The two-window method becomes critical when the element edges are located on the steep flank at the low-loss side of the spectrum (thorium $O_{4,5}$ = 88 eV, phosphorus $L_{2,3}$ = 132 eV, sulphur $L_{2,3}$ = 165 eV). However, only sulphur failed to appear, while phosphorus and thorium clearly did appear. However, the subtraction procedure at the phos-

phorus edge (and probably also the sulphur edge) suffers from the cerium and barium $N_{4,5}$ edges at 105–125 eV and 100–120 eV, respectively. So the confidence level of our phosphorus distribution image is low. Our (disputable) subtraction procedure may lead to underestimation of the area. This might be a reason why in the examples chosen (viz. cerium/phosphorus) the localizations do not completely coincide with each other. In the case of barium and cerium the now acquired neat separation might be caused by this underestimation.

The high spatial resolution in EELS analysis reported earlier [1–3,6,15] has been confirmed. In the element semi-net-intensity images shown here (fig. 1b, Th: 2.4 nm; figs. 2a–2c, Fe: 5.9 nm) and in ref. [11] (figs. 8c–8h, Ce, Ba and P: < 10 nm), the spatial element-related resolution is better than that obtained earlier with EPMA from similar material [21.23]. This improvement is not only related to EELS as an analytical tool or to the microscope system to which it is attached, but is predominantly attributable to the acquisition systems employed: TEM versus STEM. Recently, we formulated for high resolution STEM/EPMA [23] the following instrumental magnitudes, which determine the interpixel distance (IPD) at the specimen level and hence the resolution:

$$\mathrm{IPD}_{sp} = d_{sp} = \frac{d_{sc} F^*}{M N F}. \quad (1)$$

In this equation d_{sp} and d_{sc} are distances on specimen and screen, respectively, M is the magnification, N is the number of pixels (points per line) and F and F^* are reduction factors when part of the screen (F) or less than 1024 points (F^*) are used. For STEM records four lines per particle were proposed to be accepted as the minimum, resulting in a resolution of

$$d_{min} = 4\,\mathrm{IPD}_{sp}. \quad (2)$$

Accordingly, 16 pixels/particle determines the minimal accuracy.

There are no theoretical limitations to obtain high spatial resolution images with STEM systems, when a sufficiently intense field-emission source with 1 nm spot size can be used. But in practice EFEM images can be acquired at much lower magnification without sacrificing spatial resolution due to the employed post-acquisition image-analyzer system. For years, ferritin particles have been used as a test specimen [6]. Our failure to acquire iron net-intensity images from such particles in situ by EPMA/STEM analysis [23] could be attributed to the spot size/maximal intensity which can be obtained in practice with the LaB_6 cathode. Our ESI/TEM and (colloidal) particle-area analyses in element-distribution images provide arguments in favour of the combination of EFEM with a post-acquisition analyzing system, especially when the aspect of morphometric accuracy is taken into account (25 or 50 pixels/particle). However, Young calculated for the digitization of a perfect circle, analyzed in a similar way, a percentage absolute area error of 7%–8% for such low sampling densities [34].

Additional gain by EFEM acquisition can be found in the total acquisition time per digitized image, as compared to the time needed to acquire the EPMA/STEM images. We calculated for STEM/EPMA full screen 256×256 images and 1 s dwell time per pixel (point) a total acquisition time of 18.2 h [23]. One ($100\times$ integrated) shading corrected, 512×512 full screen, TEM image takes four acquisitions of about 10 s each.

Several images can be taken in a short time from the same specimen, as long as the computer image-storage capacity is not limited. However, differences in total electron dose favour the use of STEM instruments. On the other hand, the time needed to calculate true EFEM element concentration images might (in the future) take several hours, although such calculation can be performed then off-line.

An additional advantage of EFEM analyses might be the reduction of the influence of beam-broadening, by the absence of a (tilted) support film. On the other hand, element EELS quantification has just started [9,30,31]. Chelex^{100}-based Bio-standards (Bio-Rad/Polaron, Hemel Hempstead, Hertherfordshire, UK) used extensively already for EPMA analysis [2,23,19,26–29] have been shown to be as successfully applicable for EELS analysis [32,33].

In conclusion, the following statements can be made:

(a) Application of a two-window subtraction procedure results in semi-net-intensity images, if the ionization edge is far beyond the low-loss region and sufficiently high (barium, cerium, thorium). If that is not the case (sulphur) the procedure fails to result in net-intensity images. For phosphorus, in spite of the positive results, the degree of confidence of such net-intensity element distribution images is low, due to the presence of a cerium edge in the PIE window of the phosphor edge.
(b) Morphometric analysis of such semi-net-intensity element-distribution images results, after objective image segmentation, in binary element-related images from which areas or area fractions can be determined.
(c) The spatial resolution obtained in such element-distribution images from regularly and irregularly shaped particles is shown to be between 1.5 and 5.9 nm.
(d) Superposition of pseudo-colored images of multiple-element-containing precipitates is used to detect the presence (cerium and phosphorus) or absence (cerium and barium) of colocalization.
(e) The gain in accuracy following the application of image analysis with the combination Zeiss EM 902/IBAS 2000, as compared to EPMA/STEM, is related to the differences in digitization of the two systems: during image acquisition (EPMA/STEM) or after image acquisition.
(f) As a consequence of these differences, the use of the Zeiss EM 902/IBAS 2000 combination will result in:

- a high element-related spatial resolution at low magnification,
- multiple images that can be acquired in a relatively short time,
- a situation in which shading correction and noise reduction can be incorporated in the acquisition,
- a reduction of beam broadening due to the use of thin sections and the absence of a supporting film, and
- improvement of geometric accuracy due to absence of specimen tilt.

Acknowledgements

The skillful photographic and technical assistance of Mrs. Paula Delfos is gratefully acknowledged. We thank Professor Dr. J.F. Jongkind and Professor Dr. E.S. Gelsema for their valuable contributions during the experiments and the critical reading of both manuscripts.

References

[1] K.M. Adamson-Sharpe and F.P. Ottensmeyer, J. Microscopy 122 (1981) 309.
[2] A.L. Arsenault and F.P. Ottensmeyer, Proc. Natl. Acad. Sci. USA 80 (1983) 1322.
[3] A.L. Arsenault and F.P. Ottensmeyer, J. Microscopy 133 (1984) 69.
[4] L.D. Peachy, J.P. Heath and G. Lamprecht, in: Proc. 44th Annual EMSA Meeting, Ed. G.W. Bailey (San Francisco Press, San Francisco, 1986) p. 88.
[5] J. Trinick and J. Berriman, Ultramicroscopy 21 (1987) 393.
[6] N.J. Zaluzec, Ultramicroscopy 18 (1985) 185.
[7] U.B. Hezel, R. Bauer, E. Zellmann and W.I. Miller, in: Proc. 44th Annual EMSA Meeting, Ed. G.W. Bailey (San Francisco Press, San Francisco, 1986) p. 68.
[8] U.B. Hezel, R. Bauer and D. Meissner, Proc. Congr. on Electron Microscopy, Bologna, 1987, p. 64.
[9] T. Pun, J.R. Ellis and M. Eden, J. Microscopy 135 (1984) 295.
[10] R.F. Egerton, Electron Energy-Loss Spectroscopy in the Electron Microscope (Plenum Press, New York, 1986) p. 255.
[11] C.W.J. Sorber, A.A.W. de Jong, N.J. den Breejen and W.C. de Bruijn, Ultramicroscopy 32 (1990) 55.
[12] C. Colliex, C. Jeanguillaume and C. Mory, J. Ultrastruct. Res. 88 (1984) 177.
[13] C. Colliex, Ultramicroscopy 18 (1985) 131.
[14] C. Colliex, T. Manoubi and O.L. Krivanek, J. Electron Microsc. 35 (1986) 307.
[15] F.P. Ottensmeyer, J. Ultrastruct. Res. 88 (1984) 121.
[16] W. van der Meijden, H.K. Koerten, W. van Mourik and W.C. de Bruijn, Gynecol. Obstet. Invest. 25 (1988) 47.
[17] C.G. Groot, Histochemistry 71 (1981) 617.
[18] A. Müller, Ber. Dtsch. Chem. Ges. 93 (1906) 2857.
[19] L.J. Mostert, M.I. Cleton, W.C. de Bruijn, J.F. Koster and H.G. van Eijk, Int. J. Biochem. 21 (1989) 39.
[20] J.B. van Dort, J.Ph. Zeelen and W.C. de Bruijn, Histochemistry 87 (1987) 71.

[21] J.B. van Dort, G.A.M. Ketelaars, W.C. de Bruijn, Histochemistry 92 (1989) 243.
[22] W.C. de Bruijn, J. van der Meulen, P. Brederoo and W.Th. Daems, Histochemistry 84 (1986) 492.
[23] W.C. de Bruijn, H.K. Koerten, M.I. Cleton-Soeteman and C.J.G. Blok-Van Hoek, in: Scanning Electron Microscopy/1987, Ed. O. Johari (SEM, AMF O'Hare, IL, 1987) p. 1651.
[24] P. Trebbia, Proc. 1st Eur. Workshop Eur. Microbeam Analysis Soc., 1989, p. 107.
[25] D.C. Joy and D.M. Maher, J. Microscopy 124 (1981) 37.
[26] W.C. de Bruijn, in: Scanning Electron Microscopy/1981, Ed. O. Johari (SEM, AMF O'Hare, IL, 1981) p. 357.
[27] W.C. de Bruijn, Beitr. Elektronemikrosk. Direktabb. Oberfl. 16 (1981) 369.
[28] W.C. de Bruijn, J. Phys. (Paris) 45 (1984) C2-469.
[29] N. Roos and T. Barnard, Ultramicroscopy 15 (1984) 277.
[30] W.C. de Bruijn and M.P.C. van Miert, in: Scanning Electron Microscopy/1988, Ed. O. Johari (SEM, AMF O'Hare, IL, 1988) p. 319.
[31] D-R. Liu and L.M. Brown, J. Microscopy 147 (1987) 37.
[32] W.C. de Bruijn, C.W.J. Sorber, A.A.W. de Jong, J.B. van Dort, in: Proc. 1st Eur. Workshop Eur. Microbeam Analysis Soc., 1989, p. 191.
[33] J.B. van Dort, G.A.M. Ketelaars, A.A.W. de Jong and W.C. de Bruijn, Inst. Phys. Conf. Ser. 93 (1988) 577.
[34] I.T. Young, Anal. Quant. Cytol. Histol. 10 (1988) 269.